Integrative and Comparative Biology

Integrative and Comparative Biology, volume 63, number 2, pp. 332–342
https://doi.org/10.1093/icb/icad016

Society for Integrative and Comparative Biology

INVITED PAPER

Canine-inspired Unidirectional Flows for Improving Memory Effects in Machine Olfaction

Soohwan Kim[*], Sandeepan Mukherjee[*], Jordi Fonollosa [†,‡,§] and David L. Hu [*,¶,1]

[*]George W. Woodruff School of Mechanical Engineering, Georgia Institute of Technology, Atlanta, GA 30332, USA; [†]B2SLab, Departament d'Enginyeria de Sistemes, Automàtica i Informàtica Industrial, Universitat Politècnica de Catalunya, 08028 Barcelona, Spain; [‡]Networking Biomedical Research Center in Bioengineering, Biomaterials and Nanomedicine (CIBER-BBN), 28029 Madrid, Spain; [§]Institut de Recerca Sant Joan de Déu, 08950 Esplugues de Llobregat, Spain; [¶]School of Biological Sciences, Georgia Institute of Technology, Atlanta, GA 30332, USA

The first two authors contributed equally.

[1]E-mail: hu@me.gatech.edu

Synopsis A dog's nose differs from a human's in that air does not change direction but flows in a unidirectional path from inlet to outlet. Previous simulations showed that unidirectional flow through a dog's complex nasal passageways creates stagnant zones of trapped air. We hypothesize that these zones give the dog a "physical memory," which it may use to compare recent odors to past ones. In this study, we conducted experiments with our previously built Gaseous Recognition Oscillatory Machine Integrating Technology (GROMIT) and performed corresponding simulations in two dimensions. We compared three settings: a control setting that mimics the bidirectional flow of the human nose; a short-circuit setting where odors exit before reaching the sensors; and a unidirectional configuration using a dedicated inlet and outlet that mimics the dog's nose. After exposure to odors, the sensors in the unidirectional setting showed the slowest return to their baseline level, indicative of memory effects. Simulations showed that both short-circuit and unidirectional flows created trapped recirculation zones, which slowed the release of odors from the chamber. In the future, memory effects such as the ones found here may improve the sensitivity and utility of electronic noses.

Introduction

Most keen-scented mammals, such as dogs, sniff by rapidly inhaling and exhaling air in a periodic fashion. A dog's unique nasal architecture, in particular a front-facing orifice for the fluid inhale and a lateral orifice for the exhale, enables unidirectional airflow in the olfactory region. Such unidirectional airflow is thought to be a contributor to their keen sense of smell. Figure 1A shows a cross-sectional view of a dog's nasal chambers, called the ethmoidal turbinates, which increase the surface area in contact with the air, warming and humidifying it. Flow entering the nose (in red) travels along a distinct pathway from the exiting flow (in blue). Simulations of a dog's sniff have shown zones of recirculation and slow flow in the canine's olfactory pathways (Craven et al. 2007, 2010; Rygg et al. 2017). We hypothesize that these stagnant zones trap odors, giving sensors more time to identify the odors and compare them to the subsequent sniff. The objective of this study is to investigate if mimicking unidirectional airflow can enhance the performance of an artificial nose. Using an artificial nose allows for repeated controlled tests and the use of sensors to measure the local concentration of odor.

In contrast to dogs, humans have a much simpler nasal architecture that only accommodates bidirectional air flow in their olfactory region. Unlike dogs, humans have only two orifices in their nose, rather than four. Humans sniff by drawing in odor-laden air using a comparatively long and steady inhalation. Exhalation generates flow along the same path but in the opposite direction. Because flow changes directions along the same path, it has bidirectional rather than unidirectional flow. The lack of unidirectional flow is thought to

Advance Access publication April 25, 2023

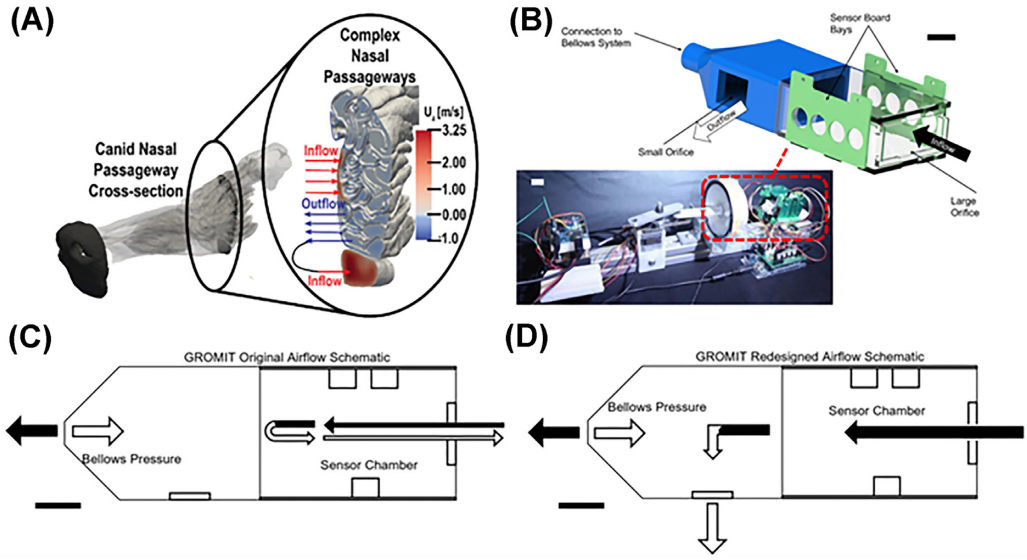

Fig. 1 Unidirectional flow in the canine and electronic nose. **(A)** Canid nasal passageway cross-section with fluid flow velocity indicated by the arrows (reprinted from Craven et al. 2007). **(B)** The original Gaseous Recognition Oscillatory Machine Integrating Technology (GROMIT) (reprinted from Spencer et al. 2021). **(C)** In the red dashed box, we place an air chamber that allows for unidirectional flow. **(C, D)** Schematic of the original and re-designed airflow chamber for GROMIT. The black and white arrows show the air flow for the inhalation and exhalation phases, respectively. All scale bars are 2 cm.

be one of the reasons why humans do not sniff to identify odors (Craven et al. 2010; Lawson et al. 2012). The idea that vertebrate nasal cavity is able to separate and sense different odors is also being investigated for other mammals like mouse (Coppola et al. 2017, 2019).

Rather than studying dogs or humans, we will study artificial noses, machines designed to identify chemicals quickly and reliably by odor. They are used in the detection of bombs, drugs, food ripeness, and food spoilage. Until such devices can be improved in sensitivity and specificity, however, many of these tasks will continue to be performed by trained humans or dogs. The first device to perform machine olfaction was built in 1964 using microelectrodes. In 1987, the term "electronic nose" was introduced to describe any device that detects odors using a sensor array (Persaud and Dodd 1982; Gardner and Bartlett 1994). Modern olfactometers involve a fan that directs steady flow to a sensory array. Staymates et al. (2016) designed a dog-nostril-inspired module that attaches to the fan and generates external airflow like that of a dog. The device improved odor acquisition and enhanced the performance of a commercial trace vapor detector compared to one that continuously drew in air. In 2021, we presented GROMIT, which used bellows to emulate the internal aerodynamics of a dog's nose, specifically the inhale and exhale of a dog's sniff (Fig. 1B, Spencer et al. 2021). While GROMIT mimicked some aspects of the pulsatile internal airflow patterns of a dog, it used bidirectional rather than unidirectional flow. The GROMIT system demonstrated tradeoffs in speed and sensitivity for ethanol detection.

In this study, we will also use ethanol vapor as the odor to be detected. Ethanol is easy to obtain, cheap, safe for human health, and causes no harm to the environment. It is commonly used for testing MOx sensors, such as in a personal robot assistant to detect gas leakages (Palacin et al. 2019) and in closed-loop control of of gas sensors (Solà-Penafiel et al. 2022).

Materials and methods

Design considerations

The 2021 GROMIT design involved a bellows system that pumped air into an airflow chamber (Fig. 1B, Spencer et al. 2021). Inside the chamber was the sensory array, and outside the device were electronics to control the air flow and read the sensors. As shown in Fig. 1C, the airflow chamber initially had two orifices: on one side was the bellows, and on the other was a single hole for incoming airflow to enter and exit the chamber. We redesigned the airflow chamber so that GROMIT has three orifices: one for the bellows and a distinct entrance and exit orifice, as seen in Fig. 1D. A dog's nose uses a clever valve-less design to drive flow unidirectionally from the inlet to the outlet, but designing such a geometry was beyond the scope of this work. Instead, we manually opened and closed the orifices.

One constraint for our design was that the volume of the airflow chamber should be equal to the volume of

the bellows itself, which was 112 mL, to enable the system to be flushed out with each sniff. Another constraint was that the chamber should be airtight. Any crevices that remained were covered in epoxy to better seal in the air. The resulting chamber consisted of two pieces, one 3D-printed and the other a rectangular prism laser cut from acrylic, with the sidewalls holding the sensors. The overall design was easy to iterate upon and repair.

Sniffing experiments

GROMIT detects odor using three commercial miniature metal oxide (MOx) sensors (TGS series, Figaro Engineering Inc., Illinois, USA) (Fig. 1C and D). A higher concentration of ethanol in the chamber generated a higher voltage reading from the sensors, measured in millivolts (mV). The MOx gas sensors are sensitive to a wide range of volatiles, such as volatile organic compounds, carbon monoxide, methane, nitrogen dioxide, and others. We installed two TGS2602 sensors and one TGS2610 in the sensor chamber. The different sensitivity of the sensors to the targeted chemicals, coupled with machine olfaction, enabled a device that can detect a large variety of chemical compounds.

We performed nine trials with GROMIT in three settings (the control, short-circuit, and unidirectional settings) shown in Fig. 2. In all settings, the bellows, shown on the left, inhaled and exhaled air in a periodic fashion. The air chamber had two orifices: a large orifice opposite the bellows and a small orifice adjacent to the bellows. The settings differed in the order in which the small and large orifices were valved open and shut. The "control" setting was how GROMIT was run in 2021 (Spencer et al. 2021). Here, the small orifice was closed, and the air traveled through the large orifice, which was kept open. The "short-circuit" setting only has the small orifice open. As a result, airflow traveled exclusively through the small orifice, effectively short-circuiting the system before it could reach the sensors. The "unidirectional" setting involved manualipulation of the orifices. We synchronized the valving with the bellows so that inhales occurred through the large orifice and exhales through the small orifice. The consequence was that fluid flow traveled unidirectionally from inlet to outlet. The unidirectional configuration was the focus of this study, and the other two settings were used as a comparison.

Each trial involved ~1–2 min of measurements. For all trials, the bellows were run at a frequency of $f = 1/3$ Hz, equivalent to a period of 3 s. This was the highest frequency that could be run without stalling out the motor that drives the bellows. The volume of the ethanol sample was re-measured before each trial to ensure evaporation effects were negligible.

Each trial began with a purge cycle, where the bellows were run for 1 min without any ethanol sample. The trial commences when 40 mL of 95% ethanol in a 50 mL beaker was placed at the inlet for 10 s. Then the ethanol sample was removed, and the bellows ran without any sample for another 30 s. The trial was complete once the sensors indicated the voltage had returned to baseline.

Mathematical modeling

The air chamber dimension was 152 × 57 × 20 mm. Considering the cross sections along its longest dimension, its hydraulic diameter $D_h = \frac{4A}{P}$ was 29.6 mm, where A is the cross-sectional area, and P is the perimeter of the cross-section. A stepper motor (Anaheim Automation Inc. 15Y202S-LW4) actuated the bellow to mimic the inhalation and exhalation of respiratory systems. The bellow consisted of an elastic annulus that started as a convex truncated cone and pushed into a concave cone. The cone had a large radius R of 38 mm, small radius r of 7.5 mm, and height h of 30 mm, with an associated volume $V_{bellow} = (1/3)\pi h(R^2 + Rr + r^2) =$ 56 mL. During an exhale, the conical bellows goes from concave to convex and thus pushes two cone volumes $2V_{bellow}$ during a half period (0.5τ), so the average flow rate during an exhale is $Q_{average} = 74.7$ mL/s. Dividing the flow rate by the cross-sectional area of the circular bellow orifice (diameter of 15.2 mm) yields the average velocity $\bar{U}_{bellow} = 0.41$ m/s. We did not verify this speed with a flow sensor because only the order of magnitude is necessary for calculating dimensionless groups. For the kinematic viscosity of the air $\nu = 1.48 \times 10^{-5}$ m^2/s and the hydraulic diameter, we obtain the Reynolds number Re and Womersley number:

$$Re_{D_h} = \frac{\bar{U}_{bellow} D_h}{\nu}, \tag{1}$$

$$Wo = D_h \sqrt{\frac{\pi f}{2\nu}}, \tag{2}$$

which produce $Re_{D_h} = 819$ and $Wo = 5.6$. The Reynolds number indicates the flow is near the turbulence regime where inertia dominates over viscosity. The Womersley number, which was originally derived to describe the cardiovascular flows (Womersley 1955), represents the ratio between the transient inertial force and viscous force. An excessive Womersley number lowers the chance for the ethanol particles to strike the sensor surface, resulting in a low signal. Previous investigators observed that the biological Womersley number across animals, including pygmy, rabbit, dog, and deer, ranges from 0.2 to 2.5 (Spencer et al. 2021). We matched the Womersley number in GROMIT by

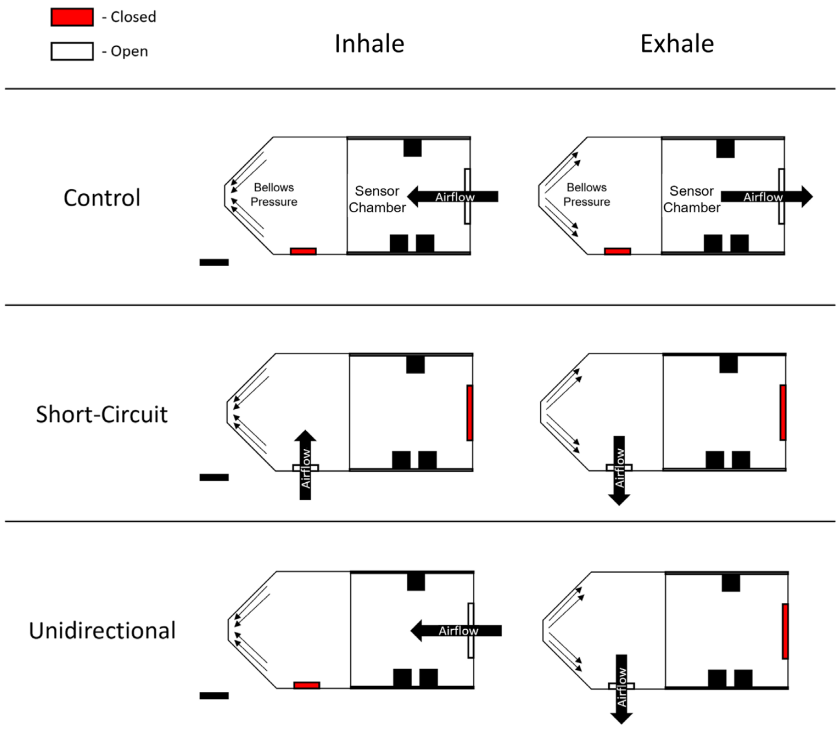

Fig. 2 Schematics for each configuration tested, with the left column showing inhalation and the right column showing exhalation. The black squares indicate the positions of the oxide sensors. A white orifice is open, and a red orifice is closed. Scale bars are 2 cm.

having a larger hydraulic diameter and a smaller frequency than in dogs. Our total bellows volume of 112 mL was chosen to be at least the same order of magnitude as the inspiratory capacity of dogs (500–2500 mL, Donati et al. 2018) while keeping our device small and easy to use.

To evaluate the effectiveness of GROMIT, we consider three metrics: the voltage drop, delay time, and residence time, illustrated in Fig. 3. The voltage drop is defined as the absolute magnitude of the largest observed change in voltage from its baseline value. The baseline voltage is the average of the voltage readings when ethanol is introduced to GROMIT's inlet. For all data, we report $t = 0$ as the time that ethanol was introduced. Furthermore, the initial voltage for all trials has been shifted to zero.

Since we provide the same ethanol concentration for each setting, a higher voltage drop indicates more ethanol exposure to the sensor. The diagonal arrows show the location of the voltage drop for each case in Fig. 3. The delay time is the time elapsed for the voltage drop to occur. A longer time delay results in longer-observed memory effects as ethanol remains trapped near the sensors. Residence time is the time that elapses before the sensor returns to within 20% of the baseline voltage. Desirable properties in a configuration are a large voltage drop, a short delay time, and a long residence time. A larger memory effect is associated with a longer residence time. Memory effects are due to the lingering particles of ethanol that remain in the chamber of the device even after the sample has been removed.

Data collection and system operation were controlled by the Arduino Uno microcontroller, as described in Spencer et al. (2021). We wrote MATLAB code to calculate the voltage drop, delay time, and residence time. We applied a median filter to the data to smooth it out using the sliding window method with a length of 10 data points.

Simulations

To better understand the flow inside the camber, we conducted two-dimensional computational fluid dynamics (CFD) simulations to characterize the time course of the velocity field and ethanol concentration field. COMSOL Multiphysics was used to find the transient solutions of the incompressible turbulence flow using the *k*-epsilon RANS (Reynolds-averaged Navier-Stokes) model. A typical time-dependent nonlinear solver was used to solve the Navier-Stokes equations, and a GMRES (Generalized Minimal Residual) solver, accelerated by a multigrid method, was used for the time marching method. A piecewise linear interpolation was used for the discretization. For incompressible

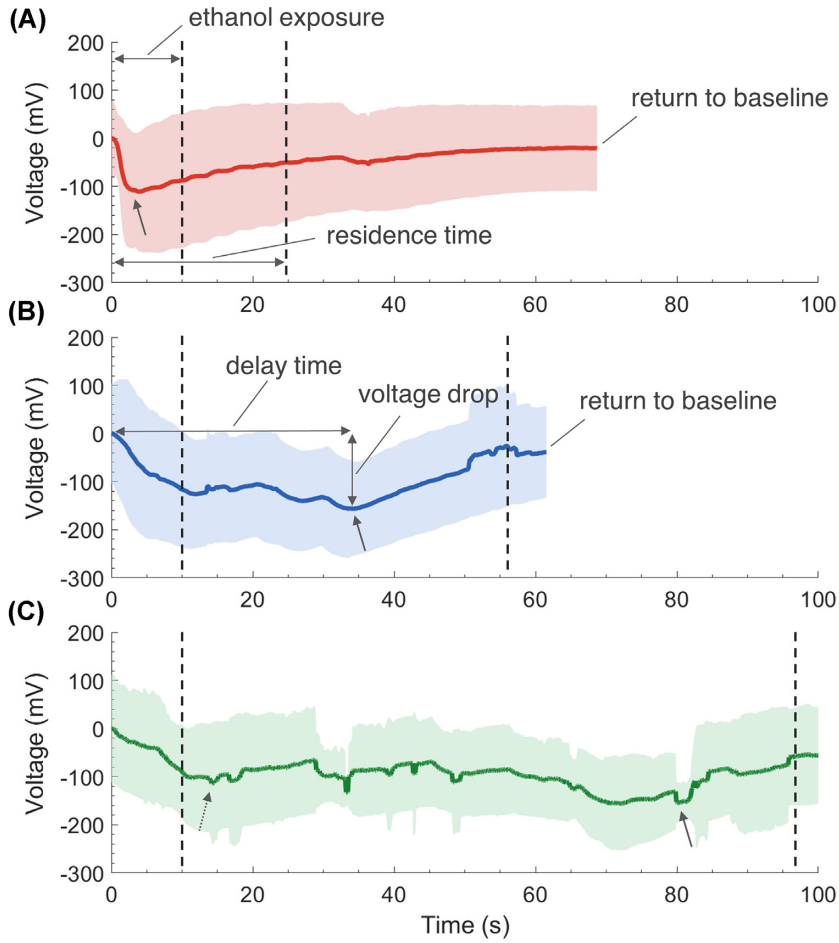

Fig. 3 Time course of sensor voltage, which indicates the level of ethanol detected. Shaded regions show the standard deviation based on three trials for each setting. Voltages have been offset to start at zero. Ethanol is introduced at $t = 0$ and removed at 10 s, as shown by the first vertical dashed line. The later vertical dashed line shows when the sensor voltage returns to baseline. **(A)** The control setting exhibits a quick initial voltage drop that begins while ethanol is still exposed to GROMIT. **(B)** The short-circuit configuration shows comparable voltage drop but longer residence time. **(C)** The unidirectional configuration exhibits a comparable voltage drop and the longest residence time of all the settings. Diagonal arrows point to the minimum voltages observed. The dotted arrow in **(C)** points to the initial voltage drop in the unidirectional setting.

Newtonian fluid flow, the Navier-Stokes equation and the continuity equation are expressed as follows:

$$\rho\left(\frac{\partial u_i}{\partial t} + u_j \cdot \frac{\partial u_i}{\partial x_j}\right) = \frac{-\partial p}{\partial x_i} + \mu\frac{\partial^2 u_i}{\partial x_j \partial x_j} + \rho f_i, \quad (3)$$

$$\frac{\partial u_i}{\partial x_i} = 0, \quad (4)$$

where ρ is the density of the fluid, u_i is the velocity component in corresponding direction, p is the pressure, μ is the dynamic viscosity, and f_i is the external force component acting on the fluid. The term on the left-hand side represents the acceleration of the fluid, and the term on the right-hand side represents the forces acting on the fluid, including pressure, viscous forces, and external forces.

The K-epsilon (k–ε) turbulence model simulates mean flow characteristics for turbulent flow conditions in CFD. This model solves for two transport equations, which are equivalent to the Navier-Stokes equation. The two transported variables are the turbulent kinetic energy k and the rate of dissipation of turbulent kinetic energy ε. The standard k–ε model has two transport equations as follows (Launder and Spalding 1983):

For turbulent kinetic energy k,

$$\rho\left(\frac{\partial k}{\partial t} + \frac{\partial\,(ku_i)}{\partial x_i}\right) = \frac{\partial}{\partial x_j}\left[\frac{\mu_t}{\sigma_k}\frac{\partial k}{\partial x_j}\right] + 2\mu_t E_{ij}E_{ij} - \rho\varepsilon. \quad (5)$$

For dissipation rate ε,

$$\rho\left(\frac{\partial \varepsilon}{\partial t} + \frac{\partial\,(\varepsilon u_i)}{\partial x_i}\right) = \frac{\partial}{\partial x_j}\left[\frac{\mu_t}{\sigma_\varepsilon}\frac{\partial \varepsilon}{\partial x_j}\right] + C_{1\varepsilon}\frac{\varepsilon}{k}2\mu_t E_{ij}E_{ij} - C_{2\varepsilon}\rho\frac{\varepsilon^2}{k}, \quad (6)$$

where E_{ij} is the component of deformation rate, μ_t is the eddy viscosity ($\rho C_\mu k^2/\varepsilon$). The k–ε model also contains adjustable constants σ_k, σ_ε, C_μ, $C_{1\varepsilon}$, and $C_{2\varepsilon}$. Empirical data fitting for a variety of turbulent flows has led to the calculations of these constants. Below are the values we used from the experimental data (Wilcox 1998).

$$\sigma_k = 1.0, \quad \sigma_\varepsilon = 1.3, \quad C_\mu = 0.09,$$
$$C_{1\varepsilon} = 1.44, \quad C_{2\varepsilon} = 1.92. \tag{7}$$

We recreated the GROMIT device in a 2D computational field based on the top view of the device, with identical chamber dimensions and dimensionless numbers ($Re = 819$ and $Wo = 5.6$). The flow simulations were conducted in two dimensions in a rectangular chamber with dimensions of 152 mm × 20 mm and a tapered end towards the bellows. As in the experimental system, there are two outlets. We defined the inlet as the boundary connected to the bellow. The outlet boundary condition was set as an open boundary, or zero atmospheric pressure, while the inlet boundary condition is an oscillating inflow velocity of $u = (\frac{\pi}{2})\bar{U}_{bellow}\sin(\frac{2\pi}{\tau}t)$. The walls of the chamber were set as having no slip boundary conditions, and the logarithmic law of the wall was configured to describe the turbulent behavior near the wall (Bradshaw and Huang 1995). While the bellow inhales or exhales the air, the outlets were set to be open boundary conditions in accordance with the timing of the setting considered. The air in the chamber was initially at rest. The system utilized a 1 mm mesh size and a time step of 0.01 s.

The transport of ethanol particles was also simulated using the Transport of Diluted Species interface in COMSOL, coupled with the velocity field obtained from the k–ε model. The massless particles follow the convection–diffusion equation given as:

$$\frac{\partial c}{\partial t} = D\frac{\partial^2 c}{\partial x_i \partial x_i} + u_i\frac{\partial c}{\partial x_i}, \tag{8}$$

where c is the concentration of the particles of interest, D is the diffusion coefficient of the particles, and u_i is the velocity component in corresponding direction. The term on the left-hand side represents the time-rate of concentration change. On the right-hand side, the first term is transport due to the diffusion governed by Fick's law, and the second term is transport owing to fluid convection. We prescribed a no flux boundary condition for the wall while following the same open boundary conditions as the turbulence model for the orifices, depending on the treatment.

The bellows boundary integrated the incoming particle flux over length and time after every inhale and pushed out the same moles of particle during exhale to emulate the transport from the bellow volume to the chamber.

One of our assumptions is that the target odor is diffusive enough in the air so that it can leave the streamline and land on the sensor. As a measure of the diffusivity of an odor, the dimensionless Schmidt number Sc may be written as follows:

$$Sc = \frac{\nu}{D}, \tag{9}$$

where ν is the kinematic viscosity of the air and D is the diffusion coefficient. In our case, the ethanol vapor in air typically has $D = 1.0 \times 10^{-5}$ m^2/s. The corresponding Schmidt number becomes 1.5, which belongs to the diffusive regime ($Sc < 4$). Our scope of study is limited to the target particles within the diffusive regime. It would be necessary to use a different technique to capture large particles such as dust, since they do not diffuse sufficiently having higher Schmidt number ($Sc \gg 1$, Cussler L. 2009).

Results

We performed nine total experiments with GROMIT, with three experiments in each of the three settings described in the methods section. Our focus was on the unidirectional flow setting, in which inflow comes through a dedicated inhale orifice and outflow goes through a separate exhale orifice, analogous to a dog's nose. We averaged readings from each of the three sensors across trials. Figure 3 shows the time course of the sensor voltage. We offset the voltage so that the baseline voltage of each sensor is zero. Figure 4 shows the averaged metrics of interest: the voltage drop (a), delay time, and residence time (b). In these figures, ethanol was exposed to GROMIT from 0 to 10 s and then removed for the rest of the trial. We first consider the control and short-circuit settings, before turning our focus to the unidirectional setting.

In the control setting, the sensors registered a swift voltage drop of 119 ± 55 mV. This voltage drop occurred at a time of 5 ± 1 s, which is faster than the short-circuit and unidirectional cases. After a 10-s exposure, the ethanol sample was removed from the inlet. Consequently, the voltage recovered to the baseline value with a residence time of 13 ± 15 s after the onset of ethanol, indicating low memory effects, as expected because the large orifice allows the chamber to be flushed clean by the bellows.

As we will show in the simulations, the short-circuit configuration generates cavity flow, whose stagnant zone might prevent the odors from reaching the sensors. Accordingly, the incoming fluid does not flow as directly to the sensors as in the control case. We see the voltage drop of 158 ± 5 mV occurs at around a time

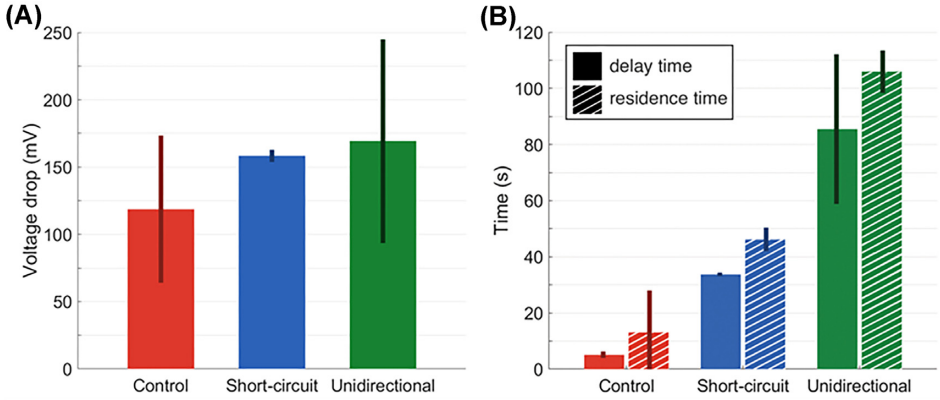

Fig. 4 Measurements of the voltage drop **(A)** and the delay and residence time **(B)** for each flow setting. The voltage drops were statistically different. The unidirectional flow showed significantly longer delay times and residence times.

of 34 ± 1 s, which is nearly six times slower than in the control setting. Moreover, a longer residence time of 46 ± 4 s is observed, indicating that the cavity flows are associated with memory effects.

The unidirectional setting showed a slower and more drawn-out response than the previous settings. The voltage drop of 169 ± 76 mV occurred at 85 ± 27 s. The voltage drop was comparable to other settings. However, the delay time was the greatest across all treatments; it was 1682% of the control and 253% of the short-circuit. The first voltage drop occurred at ∼15, as shown by the dotted arrow in the figure. Then the voltage did not return to baseline levels, but instead a second voltage drop occurred far after the ethanol sample was removed from the inlet. Finally, the signal recovered to the baseline after the residence time of 106 ± 8 s. This event was most likely a result of the bellows pushing some stagnant, odorant-laden air over the sensors again.

We conducted one-tailed *t*-tests to evaluate the statistical significance of the delay and residence times. The *t*-test showed that the delay time of the unidirectional treatment was significantly higher than both the control ($P = 0.0032$) and the short-circuit case ($P = 0.0142$). Similarly, the unidirectional residence time difference was significantly larger than both the control ($P = 0.0003$) and the short-circuit ($P = 0.0017$). The voltage drop did not show any significant differences between the three treatments ($P \gg 0.05$).

Figures 5 and 6 show our computational results with a 2D chamber of similar shape as our experiments. Figure 5A shows the internal velocity field during one cycle for each setting. Two moments were captured: inhalation ($t = 0.75$ s) and exhalation ($t = 2.25$ s). Air was sucked into the device at $t = 0.75$ s, and as can be seen by the reversal of the arrows, it had the opposite flow direction at $t = 2.25$ s. We denote the locations of two sensors by the R and L symbols. These two positions were comparable to the sensor positions in the experiment. Since the walls have a no-slip boundary condition, the distance between the wall and the reported value was 0.5 mm. Note that the left sensor position was the midpoint of the two experimental sensors at the bottom of Fig. 2.

During the exhalation, the diffuser generated flow separation and eddies near the walls. The control setting pushed the air across the sensors throughout both the inhale and exhale, as shown by the horizontal streamlines. The short-circuit setting maintained stagnation near the sensors during the entire cycle, which likely prevented the external odors from reaching the sensors. The unidirectional case pushed air to the sensors only during intake. Consequently, the introduced odor particles remained circulating in the chamber.

Figure 5B shows the time course of the air velocity in the *y*-direction for the two sensors. Later we will report odor concentration, but for now velocity indicates whether there is flow across the sensors or not. Since flow is necessary to bring odorants to the surface, we use it as a simple metric for the sensor's ability to read odors. The control setting showed the highest fluctuations in velocity, which is consistent with the velocity fields in Fig. 5A. Velocity fluctuation was the lowest in the short-circuit setting in the first cycle, but the recirculation in the short-circuit was strong enough to have comparable speed to the unidirectional case in later cycles. This implies the possibility for particles to be transported by advection in the short-circuit case. In the unidirectional configuration, the velocity fluctuation was lowest at the locations of the sensors, which may contribute to the memory effect.

We next simulated the concentration of ethanal in the chamber. During ethanol exposure, a concentration of 1 mol/m^3 boundary condition was used for the incoming air for an initial three cycles, which had a comparable duration of exposure (9 s) to the experiment (10 s). After

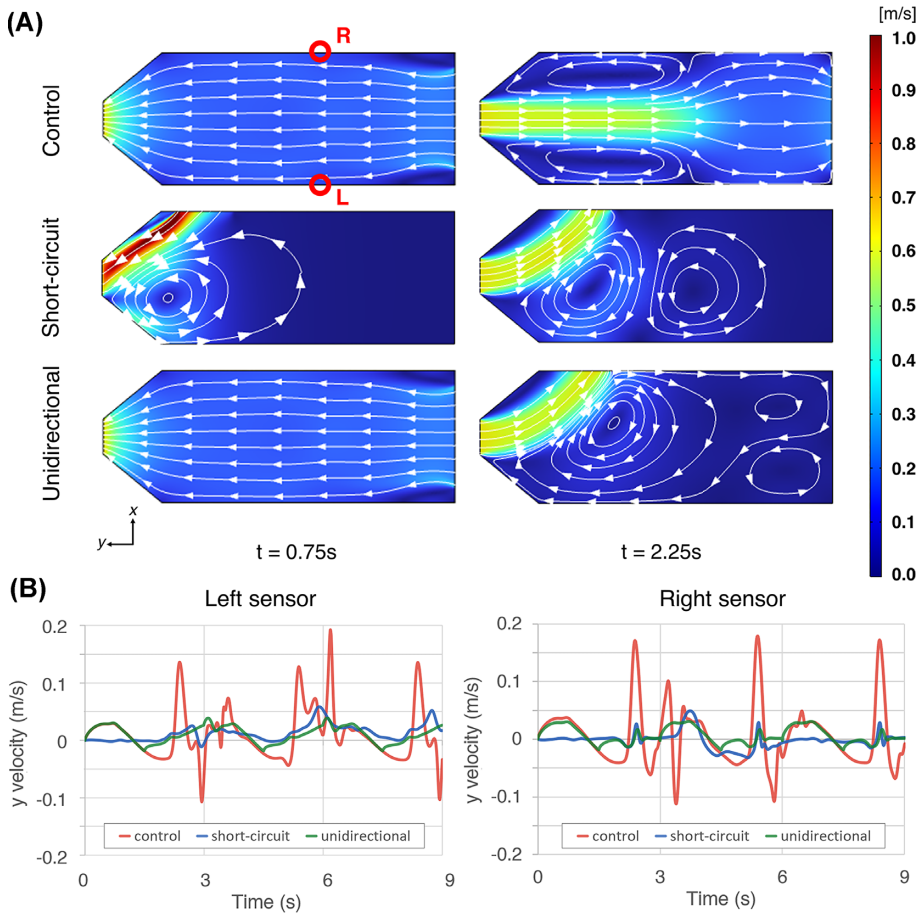

Fig. 5 (A) Simulations showing two snapshots of the velocity field for three flow settings. Air is inhaled at $t = 0.75$ s, changes flow direction, and is exhaled at $t = 2.25$ s. A cycle is 3 s long. **(B)** Velocity in the y-direction at two points marked with red circles in **(A)** where sensors are located. The left wall sensor (left panel) and right wall sensor (right panel) are each located 60 mm above the bottom of the chamber. Red curve is control, blue is the short-circuit setting, and green is the unidirectional setting.

the exposure, the system operated without an influx of ethanol for an additional 17 cycles, which is equivalent to 60 s of operation in total.

Figure 6A shows the simulated ethanol concentration field at the same moments as Fig. 5A. The red color indicates a high concentration of ethanol. During inhalation ($t = 0.75$ s), the ethanol entered the inlet of each setting, and the bellow also inhaled a portion. During exhalation ($t = 2.25$ s), the bellow exhaled its contents, driving flow towards the respective outlet for each setting. Note that the control case flushed out ethanol during the exhale, with only some ethanol remaining near the walls of the diffuser. We expected the short-circuit case to introduce little ethanol into the chamber. That was mostly the case, but diffusive transport still entrained ethanol into the circulation region on the right. The unidirectional case had an identical concentration to the control during the inhale. However, the exhale to the nearby outlet permitted a much higher concentration of particles to reside in the chamber, demonstrating the memory effect.

We integrated the concentration across the chamber area to find the total amount of ethanol per unit depth. If sensors were equipped all over the chamber, this average concentration could be measured and compared to experiments. However, in our experiments, sensors were only placed on the right-hand side of the chamber. Figure 6B shows the time course of ethanol during 20 cycles, equivalent to 60 s. The initial three cycles were exposed to an incoming ethanol-laden flow of 1 mol/m^3 of concentration.

The control case (in red) showed the largest fluctuation in concentration throughout the cycles, followed by the unidirectional case (in green). Both of these settings were the most responsive; they increased to their peak concentration within a single cycle. In comparison, the short circuit flow had the slowest ethanol entrainment into the chamber; it took nearly three cycles to obtain the same level of ethanol as the other settings. After the ethanol was removed, the unidirectional and control cases showed the most rapid decay to zero concentration, followed by the short circuit case. Thus, the

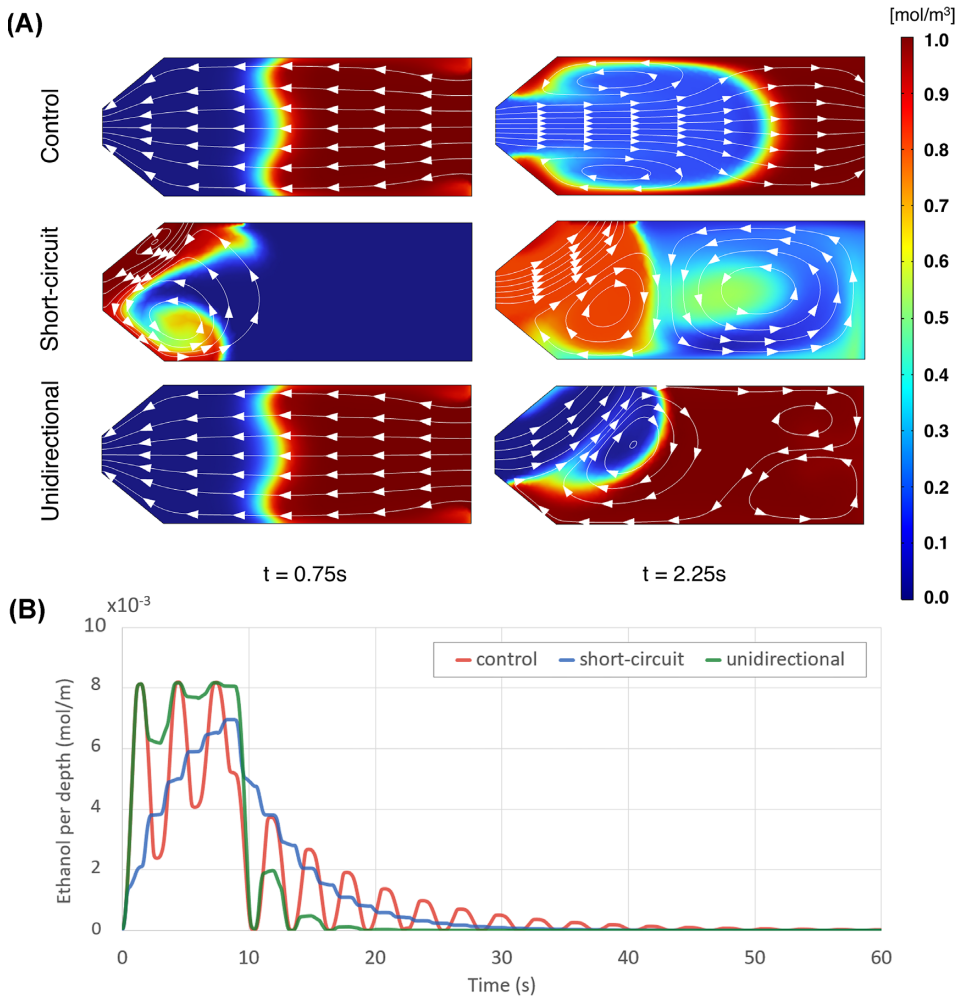

Fig. 6 (A) Simulations of the ethanol concentration field for the three flow settings at two points in time: $t = 0.75$ s and $t = 2.25$ s. White arrows show streamlines. **(B)** Simulations of the time course of ethanol concentration (number of moles of ethanol per unit depth). Red is the control, blue is the short-circuit setting, and green is the unidirectional setting.

simulations show that the short circuit setting had the highest memory effect when considering the entire chamber.

Discussion

In this study, we considered the memory effect—the ability of systems to maintain previous odors—over subsequent sniffs. We hypothesize that this ability is advantageous to animals because it would facilitate comparison of current and previous sniffs. The ability of a system to hold its memory was affected by the timing of the openings of the orifice and their size and position. In both the short-circuit and unidirectional flow settings, exhaled air is pushed towards the large orifice, which is blocked. The small orifice on the side requires fluid to change direction and has a small hole. Thus, odor-laden air faces infinite resistance exiting the large orifice and high resistance exiting the small orifice. This resistance generates the ensuing stagnation zones, which cause some of the odorant to remain within the chamber and continue to interact with the sensors. The longer the sample is exposed to the sensors, the stronger and more extended the voltage change. Indeed, in our experiments, we saw that the unidirectional setting had the longest delay and residence time.

Figure 3A shows that the control configuration starts to decrease during ethanol exposure. In this configuration, we expect a voltage drop during the inhale, followed by a voltage recovery during the subsequent exhale. Indeed, simulation shows this while ethanol is present. However, our experiments do not show these oscillations in voltage. The sensors have a small metallic housing to prevent physical damage. We surmise that the sensor housing smooths these oscillations.

We were surprized that the simulations (Fig. 6B) showed that the short circuit configuration had the

longest decay time and thus the largest memory effect. From the experiments, we expected the unidirectional setting to have the largest memory effect. The difference might be explained by sensor sensitivity. The short-circuit case has the strongest memory effect if the sensor's limit of detection is above ∼2 mol/m, and the unidirectional case has the strongest memory effect if the limit of detection is above ∼7 mol/m. Therefore, characterizing the sensor's sensitivity would help to rationalize the experimental and computational results.

In nature, the observed memory effect allows animals to scan for gradients in odor across different locations or make comparisons of mixtures of odor from one location to another. The ability to retain the sample and expose sensors for a longer duration should also help electronic noses detect odor concentrations near their limit of detection.

We briefly discuss the limitations of our study. Our tests only use ethanol, whereas in nature, odors will be combinations of different chemicals. Additionally, our device does not have a liquid coating analogous to the mucus of the biological nose, which would require even more time for odorant molecules to diffuse through. In natural noses, different odors land on different portions of the olfactory epithelium, an effect termed odorant partitioning or differential sorption. Our work is thus most applicable to sniffing relatively insoluble odors, which are deposited rather uniformly along mucus-lined olfactory airways. Our chamber design is very simplified in comparison to the tortuous nasal cavity of dogs, whose small channels could further amplify the memory effects found here.

Conclusion

The goal of this study was to determine the benefits of unidirectional flow on olfaction. We designed and built a unidirectional flow chamber that was incorporated into the pulsatile electronic nose, GROMIT. We studied three settings for the flow circuit that affected the odor retention in the chamber. All settings had comparable levels of voltage drop in response to the odor; in other words, they sensed the same concentration of the odor. However, the unidirectional flow's sensing was more stretched out: it had the longest delay time until the voltage drop and the longest time to return to baseline. This is a demonstration of a physical memory by which circulation zones maintain odors for longer than a single cycle of sniffing. Our simulations also show that in these stagnant zones, the concentration of odors is higher, consistent with the greater signal intensity recorded by our oxide sensors. This work brings artificial noses one step closer to being more useful and robust in complex environments.

Acknowledgments

We thank Brent A. Craven for suggesting this direction of study and contributing throughout.

Funding

This work was supported by the President's Undergraduate Research Awards (PURA) grant from Georgia Institute of Technolgy and NSF Physics of Living Systems (PoLS). This work was supported by the Spanish Ministry of Economy and Competitiveness (www.mineco.gob.es) PID2021-122952OB-I00, DPI2017-89827-R, Networking Biomedical Research Centre in the subject area of Bioengineering, Biomaterials and Nanomedicine (CIBER-BBN), initiatives of Instituto de Investigación Carlos III (ISCIII), Share4Rare project (Grant Agreement 780262), ISCIII (grant AC22/00035), ACCIÓ (grant Innotec ACE014/20/000018) and Pla de Doctorats Industrials de la Secretaria d'Universitats i Recerca del Departament d'Empresa i Coneixement de la Generalitat de Catalunya (2022 DI 014). JF also acknowledges the CERCA Program/Generalitat de Catalunya and the Serra Húnter Program. B2SLab is certified as 2017 SGR 952.

Supplementary data

Supplementary data available at *ICB* online.

Conflict of interest

We declare we have no competing interests.

Data availability

Raw data were generated at Georgia Tech. Derived data supporting the findings of this study are available from the corresponding author (DH) on request.

CFD simulation movies

Movie 1: Velocity field of the Control Setting (Case 1)

Movie 2: Velocity field of the Short Circuit Setting (Case 2)

Movie 3: Velocity field of the Unidirectional Setting (Case 3)

Movie 4: Concentration field of the Control Setting (Case 1)

Movie 5: Concentration field of the Short Circuit Setting (Case 2)

Movie 6: Concentration field of the Unidirectional Setting (Case 3)

References

Bradshaw P, Huang GP. 1995. The law of the wall in turbulent flow. Proc Royal Soc London A Math Phys Sci 451:165–88.

Coppola DM, Fitzwater E, Rygg AD, Craven BA. 2019. "Tests of the chromatographic theory of olfaction with highly soluble odors: a combined electroolfactogram and computational fluid dynamics study in the mouse". Biol Open 8:bio.047217. https://doi.org/10.1242/bio.047217.

Coppola DM, Ritchie BE, Craven BA. 2017. "Tests of the sorption and olfactory 'fovea' hypotheses in the mouse". J Neurophysiol 118:2770–88. https://doi.org/10.1152/jn.00455.2017.

Craven B, Paterson E, Settles G. 2010. The fluid dynamics of canine olfaction: unique nasal airflow patterns as an explanation of macrosmia. J R Soc, Interface 7:933–43.

Craven BA, Neuberger T, Paterson EG, Webb AG, Josephson EM, Morrison EE, Settles GS. 2007. Reconstruction and morphometric analysis of the nasal airway of the dog (*Canis familiaris*) and implications regarding olfactory airflow. Anat Rec (Hoboken) 290:1325–40.

Cussler EL. 2009. Diffusion: Mass Transfer in Fluid Systems. Cambridge: Cambridge University Press.

Donati PA, Gogniat E, Madorno M, Guevara JM, Guillemi EC, Lavalle MDC, Scorza FP, Mayer GF, Rodriguez PO. 2018. Sizing the lung in dogs: the inspiratory capacity defines the tidal volume. Revista Brasileira de Terapia Intensiva 30: 144–52.

Gardner JW, Bartlett PN. 1994. "A brief history of electronic noses". Sens Actuators, B 18:210–11. https://doi.org/10.1016/0925-4005(94)87085-3.

Launder BE, Spalding DB. 1983. The numerical computation of turbulent flows. In: Numerical Prediction of Flow, Heat Transfer, Turbulence and Combustion. Pergamon: Oxford. p. 96–116

Lawson MJ, Craven BA, Paterson EG, Settles GS. 2012. "A computational study of odorant transport and deposition in the canine nasal cavity: implications for olfaction". Chem Senses 37:553–66. https://doi.org/10.1093/chemse/bjs039.

Palacín J, Martínez D, Clotet E, Pallejà T, Burgués J, Fonollosa J, Pardo A, Marco S. 2019. Application of an array of metal-oxide semiconductor gas sensors in an assistant personal robot for early gas leak detection. Sensors 19: 1957.

Persaud K, Dodd G. 1982. Analysis of discrimination mechanisms in the mammalian olfactory system using a model nose. Nature 299:352–5. https://doi.org/10.1038/299352a0.

Rygg AD, Van Valkenburgh B, Craven BA. 2017. The influence of sniffing on airflow and odorant deposition in the canine nasal cavity. Chem Senses 42:683–98.

Solà-Penafiel N, Manyosa X, Navarrete E, Ramos-Castro J, Jimenez V, Bermejo S, Gracia I, Llobet E, Domínguez-Pumar M. 2022. Acceleration and drift reduction of MOX gas sensors using active sigma-delta controls based on dielectric excitation. Sens Actuators, B 365:131940.

Spencer TL, Clark A, Fonollosa J, Virot E, Hu DL. 2021. Sniffing speeds up chemical detection by controlling air-flows near sensors. Nat Commun 12:1232.

Staymates ME, MacCrehan WA, Staymates JL, Kunz RR, Mendum T, Ong T-H, Geurtsen G, Gillen GJ, Craven BA. 2016. Biomimetic sniffing improves the detection performance of a 3D printed nose of a dog and a commercial trace vapor detector. Nat Sci Rep 6:36876.

Wilcox DC. 1998. Turbulence Modeling for CFD. Vol. 2. La Canada (CA): DCW Industries. p. 103–217.

Womersley JR. 1955. Method for the calculation of velocity, rate of flow and viscous drag in arteries when the pressure gradient is known. J Physiol 127:553.